

Synaptic input statistics tune the variability and reproducibility of neuronal responses

Alan D. Dorval II^{a)} and John A. White

Department of Biomedical Engineering, Center for BioDynamics, Center for Memory and Brain, Boston University, Boston, Massachusetts 02215

(Received 3 February 2006; accepted 10 May 2005; published online 30 June 2006)

Synaptic waveforms, constructed from excitatory and inhibitory presynaptic Poisson trains, are presented to living and computational neurons. We review how the average output of a neuron (e.g., the firing rate) is set by the difference between excitatory and inhibitory event rates while neuronal variability is set by their sum. We distinguish neuronal variability from reproducibility. Variability quantifies how much an output measure is expected to vary; for example, the interspike interval coefficient of variation quantifies the typical range of interspike intervals. Reproducibility quantifies the similarity of neuronal outputs in response to repeated presentations of identical stimuli. Although variability and reproducibility are conceptually distinct, we show that, for ideal current source synapses, reproducibility is defined entirely by variability. For physiologically realistic conductance-based synapses, however, reproducibility is distinct from variability and average output, set by the Poisson rate and the degree of synchrony within the synaptic waveform. © 2006 American Institute of Physics. [DOI: 10.1063/1.2209427]

Cortical neurons receive thousands of excitatory and inhibitory synaptic inputs per second, each constituting a small conductance change coupled with a synaptic reversal potential. According to some encoding scheme that is still a subject of study, neurons convert their synaptic inputs into trains of action potentials. In this work, we review the relationships between standard synaptic input parameters and the neuronal outputs they produce. We focus on three measures of output: average output responses (membrane potential or spike rate), the temporal variability of responses, and the reproducibility of responses to repeated presentations of “frozen noise” inputs. We contrast these measures in response to experimentally convenient current-based inputs and more realistic conductance-based inputs. With current-based inputs, we find that the mean firing rate and variability can be tuned independently with simple input structures, but that reliability is not independently tunable. In contrast, conductance-based inputs enable a richer output space in which spike rate, variability, and reliability can be independently tuned using simple synaptic inputs.

I. INTRODUCTION

A neuron receives information from upstream nerve or sensory cells, restructures that information, and passes it along to downstream neurons or muscles cells. Depending on the physiological and situational details of the neuron, that restructuring step takes one of many forms: signals can be relayed, recorded, summed, subtracted, multiplied, multiplexed, divided, differentiated, integrated, or ignored. From the information processing perspective, however, signal re-

structuring can be summarized with thorough input-output (I/O) maps. The typical output of interest is the membrane potential—in particular, the occurrence of action potentials.

Whether the average spike rate or precise spike timing is more important is an ancient, enduring debate in the neuroscience community. An emerging picture is that both measures matter: the average spike rate conveys significant information but the specific pattern of spike times may be equally important. If patterns of spikes are to convey any useful information, they must be reproducible. That is, a neuron should respond similarly to repeated presentations of the same input. However, responses to repeated identical sensory stimuli *in vivo* can be highly unreliable.^{1,2} This finding suggests that if firing patterns matter at all, physiologically realistic I/O maps should assign probability values to various outputs as a function of input. A thorough exploration of these maps should include the inputs that a neuron likely receives in its natural state. The synaptic inputs that drive responses *in vivo* can be significantly synchronized,^{3,4} with a degree of synchronization that can be modulated by attention⁵ and local rhythms.^{6–8} Synaptic correlations following from presynaptic synchrony alter the synaptic waveform and consequently the output statistics of the postsynaptic neuron.^{9,10}

Here, we focus on the effects of specific features of fluctuating synaptic inputs on the features of neuronal output, in both neuronal recordings and in a simple neuronal model. In doing so, we operate from the viewpoint that fluctuating background activity is not “synaptic noise” but rather part of the complex signal to which the neuron is meant to respond. We examine neuronal outputs in response to synaptic inputs that, after being generated via a probabilistic process, are frozen and presented to a neuron many times. Given this frozen synaptic input, a neuron has an ideal response, i.e., the

^{a)}Present address: Department of Biomedical Engineering, Duke University, Durham, North Carolina 27708.

output in the absence of all other noise sources. In real neurons, however, both extrinsic and intrinsic noise sources keep neuronal output from exactly reflecting the idealized response. Extrinsic noise sources are primarily true synaptic noise, which may stem from many sources, including presynaptic action potential propagation failure, probabilistic vesicle release,¹¹ variable vesicle size,¹² probabilistic receptor binding, and spurious presynaptic spike generation.¹³ Intrinsic noise sources include the stochastic effects of ion-channel flicker, which can be large enough to alter neuronal output.^{14,15} Because we deliver inputs via the recording electrode, our approach eliminates extrinsic noise, leaving only intrinsic noise to induce unreliable responses (i.e., responses that differ from trial to trial).

The inputs used in this study are simple. Excitatory and inhibitory inputs are driven by separate homogeneous Poisson processes. We vary the degree of presynaptic synchrony by altering the size of the postsynaptic input induced by each presynaptic event. Because biological synaptic inputs arise via changes in postsynaptic conductance, and because neuronal responses differ substantially with current-based and conductance-based synaptic background inputs,^{16–18} we compare responses generated by these two input modalities. Conductance-based inputs are delivered experimentally using the dynamic clamp technique.^{19–21}

Our analysis of modeled and measured outputs focuses on three measures: output mean, variability, and reproducibility. With theoretical results, simulations, and experimental recordings, we demonstrate that our simple input structure has the flexibility to span the physiologically relevant space of output mean and variance, for both conductance-based and current-based inputs. For current-based inputs, there is a one-to-one correspondence between variability and reproducibility—more highly variable outputs are also more reproducible. Conductance-based inputs, however, provide additional flexibility by enabling the independent tuning of variability and reproducibility. For a fixed firing rate in either modality, output patterns may be highly variable and highly reproducible, or minimally variable and minimally reproducible. However, for the conductance input modality only, output patterns may also be minimally variable but highly reproducible, or the converse.

II. METHODS

For this work, we utilized both computational and experimental methods. We presented similar stochastic pseudosynaptic waveforms to both integrate-and-fire models and neurons living in a brain slice preparation. In this section we detail the construction of the pseudosynaptic waveforms, the modeling of the integrate-and-fire neurons, the tissue preparation, and the methods we used to present the stochastic waveforms *in vitro*.

A. Synaptic input waveforms

Many theoretical and computational studies have explored how different models of synaptic inputs affect neuronal responses. One often overlooked detail is the input modality: whether synapse are modeled as ideal current sources

or as a more biologically realistic conductance in series with a synaptic reversal potential. In this work we present identical frozen pseudosynaptic inputs to computational and *in vitro* neurons as both currents and conductances.

In either input modality, the synaptic waveform is a random process that we will model to generate the frozen pseudosynaptic inputs. This random process is often modeled as some Gaussian distributed waveform: either white noise (which in the current modality can yield qualitatively incorrect results)²² or an Ornstein-Uhlenbeck source.¹⁷ In the conductance modality these approaches are perfectly valid for evaluating input-output relationships, but they lack a notion of synaptic identity. Hence, questions concerning how synaptic strength or release rate affect output statistics are difficult to address.

Another common approach, and the one taken in this paper, is to consider input as a synaptic kernel convolved with an event train, typically generated from a Poisson process. In this general construction the kernel represents the signal delivered to the neuron by an individual synapse, and each element of the event train represents a presynaptic spike. Previous work has explored the case of exponentially decaying synapses²² ($e^{-t/\tau}; t \geq 0$) and alpha function synapses²³ ($te^{-t/\tau}; t \geq 0$). The general findings of these approaches are similar. We will focus on a difference-of-exponentials kernel ($e^{-t/\tau_f} - e^{-t/\tau_r}; t \geq 0$). The difference-of-exponentials incorporates the independent rising and falling time constants observed experimentally, τ_r and τ_f , respectively. Our input waveform model is thus a Poisson process, characterized by a Poisson rate λ , convolved with a difference-of-exponentials function (Fig. 1). In addition, we scale the difference-of-exponentials function by N representing the number of synapses that fire synchronously with each independent event. Further explained in the results, high values of N enable the variable firing patterns observed *in vivo*.²⁴

The average synaptic rate is thus $f = \lambda N$. While the average value of the input waveform is proportional to f , the variability is differentially affected by changes to λ and N (Fig. 2). Specifically, the variance is proportional to λ and N^2 . In computational models we explore the effects of these parameters on neuronal behavior. Because input variability is more sensitive to N , we focus our *in vitro* work on neuronal properties as a function of N in order to restrict our experimental studies to a reasonable number of trials.

B. Computational modeling

The pseudosynaptic waveforms described previously were generated at run time with a fixed time step Δt , set to 10 μs for computational models and 75 μs for living neurons. We used a formulation that can be calculated in a fixed number of steps (a real-time computing requirement for the *in vitro* case) while accommodating arbitrarily many difference-of-exponentials synaptic events of the same type with only two state variables and requiring only one pseudorandom number per time step. For each Poisson rate λ , a cumulative distribution function was constructed and inverted, such that all numbers from 0 and 1 could be mapped

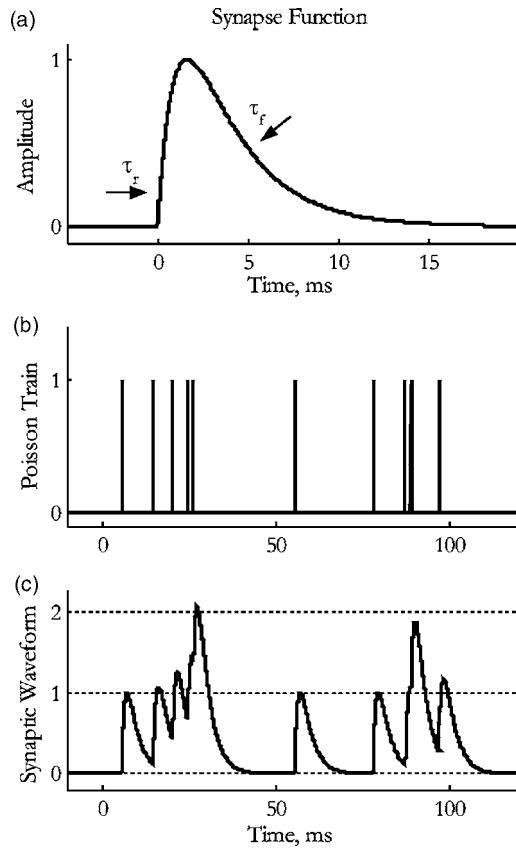


FIG. 1. Pseudosynaptic waveform. Construction of the pseudosynaptic waveform used to simulate neuronal inputs received *in vivo*. (a) The shape of the individual synapse function is a difference of exponentials. The synapse onset is dominated by the rising time constant ($\tau_r=1$ ms), and the synapse decay is controlled by the falling time constant ($\tau_f=3$ ms). A simple normalization procedure keeps the peak amplitude at unity: defining $A \equiv (\tau_r/\tau_f)^{1/(\tau_f-\tau_r)}$, divide the waveform amplitude by $(A^{\tau_r}-A^{\tau_f})$. (b) Example realization of a Poisson process with characteristic rate $\lambda=100$ Hz. (c) The pseudosynaptic waveform is the convolution of the difference-of-exponentials synapse function with the Poisson train.

into an integer number of events. A uniformly distributed pseudorandom number from 0 to 1 was generated for each time step and mapped back into the inverted distribution function to yield the number of events $m(k)$ in time step k , typically zero or one. Rising and falling synaptic variables (a_r and a_f) were incremented by the number of new events and allowed to decay exponentially. The amplitude $s(k)$ at each k was found as the difference of synaptic variables scaled by N , the number of synapses per event,

$$\begin{aligned}
 a_r(k+1) &= a_r(k)e^{-\Delta t/\tau_r} + m(k), \\
 a_f(k+1) &= a_f(k)e^{-\Delta t/\tau_f} + m(k), \\
 s(k) &= N[a_f(k) - a_r(k)].
 \end{aligned}
 \tag{1}$$

The time signal $s(t)$ was constructed as a zeroth-order hold of $s(k)$ [i.e., $s(t)=s(k)$ for $t_k \leq t < t_{k+1}$]. We kept the waveforms similar by using identical random seeds for various trials. With this method, trials with identical Poisson rates λ but different N are precisely scaled versions of one another and trials with different λ are highly correlated. This correlation can be understood by ranking time bins by their re-

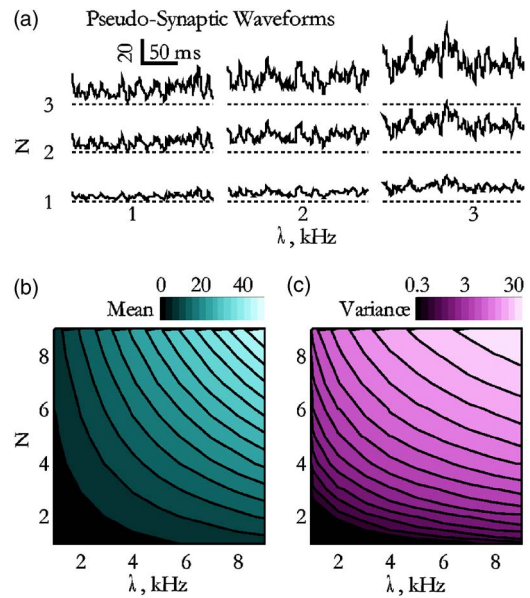


FIG. 2. Poisson rate vs synchrony. Pseudosynaptic waveforms were generated while varying the Poisson rate λ and the number of synchronous synaptic releases N per element of the Poisson train. (a) Example realizations for three values of N and λ . The vertical scale is unitless; a value of 1 is the peak amplitude of a single synaptic event; the dotted lines indicate 0. For a visually fair comparison, each trial was simulated from the same random number series. Hence, trials in a column are literally scaled versions of each other and trials in a row are highly correlated. Note that the corners $\{N, \lambda\} = \{3, 1\}$ and $\{1, 3\}$ have identical means but that the variability is much larger in the former. (b) The mean waveform amplitude is identically dependent upon N and λ . (c) Waveform variance is more sensitive to changes in N than λ . Note the logarithmic color scale.

spective pseudorandom numbers, r_1 to r_k . Because cumulative distribution functions are necessarily monotonic, smaller pseudorandom numbers correspond to fewer events: $m(r_1) \leq m(r_2) \leq \dots \leq m(r_k)$. The rank order of the number of events in each bin will never change, meaning waveforms with different values of λ will exhibit similar peaks and valleys.

The dimensionless waveform $s_x(t)$ represents all synaptic inputs of a given type x (e.g., excitatory or inhibitory). To present the pseudosynaptic inputs to a neuron, s_x was converted to a current I_x in one of two ways depending on the modality being modeled. For the current input modality, I_x is

$$I_x(t) = \frac{Q_x}{\tau_f - \tau_r} s_x(t),
 \tag{2}$$

where Q_x is the total charge delivered per event. A common alternate approach is to scale each unitary synaptic event by a peak current value, I_{peak} . The approaches are equivalent with $I_{\text{peak}} = Q_x/[S_\tau(\tau_f - \tau_r)]$, where the charge normalization parameter, $S_\tau \equiv (A^{\tau_r} - A^{\tau_f})$ with $A \equiv (\tau_r/\tau_f)^{1/(\tau_f-\tau_r)}$, is completely determined by the time constants. For the conductance modality, the current was found as

$$I_x(t) = \frac{\Phi_x}{\tau_f - \tau_r} [V_x - V_m(t)] s_x(t),
 \tag{3}$$

where Φ_x is the conductance-modality analog of charge, V_x is the synaptic reversal potential, and V_m is the time varying membrane potential. In parallel with the current modality

case, the peak unitary conductance is $G_{\text{peak}} = \Phi_x / [S_\tau(\tau_f - \tau_r)]$. Regardless of the modality, the total synaptic input I_{syn} typically comprised one type of excitatory I_e and inhibitory I_i pseudosynaptic waveform: $I_{\text{syn}}(t) = I_e(t) + I_i(t)$.

For computational experiments we used a passive membrane parametrized by a capacitance C_m and leak conductance G_m (yielding a time constant $\tau_m = C_m / G_m$), and rest potential V_{rest} ,

$$\frac{dV_m}{dt} = \frac{1}{\tau_m} [V_{\text{rest}} - V_m(t)] + \zeta(t) \sqrt{D_m} + \frac{1}{C_m} I_{\text{syn}}(t) \quad (4)$$

with the synaptic waveforms that comprise $I_{\text{syn}}(t)$ defined previously. The noise term $\zeta(t)$ denotes a zero mean, unit variance, white noise process, weighted by the square root of the potential diffusion coefficient D_m . This diffusion coefficient can be set to determine membrane noise variance $\eta_{V_m}^2$ in the absence of synaptic input, by the relationship: $D_m = 2\eta_{V_m}^2 / \tau_m$. In the noise free case, the one dimensional model of Eq. (4) was solved analytically for V_m at each time step of $I_{\text{syn}}(t)$ with D_m at zero. When including noise, a stochastic term equal to $\xi(k)(\Delta t D_m)^{1/2}$ was added to each $V_m(k)$ before progressing to the next time step, where each $\xi(k)$ is an independent, zero-mean, unit-variance Gaussian pseudorandom number.

Parameters were selected to approximate their physiologically measured counterparts in the superficial entorhinal cortex: $C_m = 100$ pF, $G_m = 10$ nS. The system is invariant to shifts in V_{rest} , which was set to 0 for simplicity. When spiking behavior was desirable, we turned the passive model into an integrate-and-fire neuron by introducing a threshold V_{th} . Whenever V_m exceeded V_{th} , a spike occurred and V_m was held at V_{reset} for an absolute refractory period of 10 ms. Shifted by the rest potential, V_{th} and V_{reset} were set to 10 mV and -10 mV, respectively.

C. Biological methods

Experiments were conducted as approved by the Boston University Institutional Animal Care and Use Committee according to established techniques. Briefly, Long-Evans rats between days 12 and 22, were anesthetized by overexposure to CO₂ and euthanized via guillotine. The skull was opened and the brain immediately immersed in 0°C artificial cerebral spinal fluid (ACSF). The ACSF consisted of, in mM: NaCl 126, KCl 3, NaH₂PO₄ 1.25, MgSO₄ 2, NaHCO₃ 26, D-Glucose 10, CaCl₂ 2. It was buffered to a pH of 7.4 with 95/5% O₂/CO₂. Immersed in ACSF, the brain was glued to a slicing chamber. Horizontal slices containing the hippocampus and entorhinal cortex were cut to a thickness of 350–400 μm using a horizontal slicer (1000+, Vibratome). Seven to ten slices per animal were placed in a room temperature bubble chamber, continuously bathed in oxygenated ACSF. Slices were allowed to recover for 1.5 h prior to experimental recordings.

Electrodes were pulled on a horizontal puller (P97, Sutter Instruments) and filled with artificial neuroplasm containing, in mM: K-gluconate, 135; HEPES 10.0; NaCl 5.0; MgCl₂ 2.0; EGTA .50; Tris-ATP 2.0; Tris-GTP 0.40. KOH was added to reach a pH of 7.25. Final electrode resistances

were between 3.5 and 7.0 M Ω . Tissue slices were moved from the bubble chamber to the stage of an infrared, differential interference contrast equipped microscope (Axioskop 2+, Zeiss). The microscope stage was bathed in recycling oxygenated ACSF with 10 μM CNQX, 10 μM bicuculline methiodide, and 30 μM AP-5 added to block all ionotropic synaptic activity. Healthy principal neurons within layer II of the medial entorhinal cortex were visualized.

Electrodes were attached to the headstage of a current clamp amplifier (either the AxoClamp 2B or the Multiclamp 700A, both from Axon Instruments), connected to a standard personal computer via a multipurpose data acquisition card (E-series, National Instruments). Electrode tips were patched onto neuronal membranes with G Ω seals with a manual (Huxley) or electronic (S. D. Instruments) micromanipulator and mild suction. Pulses of strong suction fractured the membrane patch. Neurons were hyperpolarized to -70 mV for at least one minute while the bridge and capacitance compensation were set. Data were recorded on the computer at sample rates between 5 and 20 kHz (typically 13.3 kHz). Neurons that exhibited a greater than 20% membrane potential sag to hyperpolarizing current pulses were identified as stellate neurons.²⁵ All other cells were labeled pyramidal neurons. After identification, cells were allowed to rest for ten minutes prior to experimental recordings.

D. Synaptic waveform delivery

We delivered identical pseudosynaptic currents $I_{\text{syn}}(t)$ to computational and living neurons as both currents and conductances. Exponential time constants were $\tau_r = 1$ ms and $\tau_f = 3$ ms, and did not vary between modality or synapse type. Although inhibitory synapses are typically slower than excitatory ones *in vivo*, keeping identical time constants simplifies the presentation of results without changing the general findings. To generate and deliver both input modalities to living neurons, we used a dynamic clamp system running under Real-Time Application Interface for Linux.¹⁹ All *in vitro* inputs were strictly excitatory. For the current modality, $Q_x = 10$ fC. In the conductance modality, we set excitatory synaptic reversal potential to $V_x = 0$. The conductance modality amplitude was set to match the current modality at rest [by Eqs. (2) and (3): $Q_x = \Phi_x(V_x - V_{\text{rest}})$] and depended on the rest potential in units of mV: $\Phi_x = -10$ fC/ V_{rest} . The same parameters were used for the computational models, except since V_{rest} had been shifted to zero, we defined $\Phi_x = 0.2$ fC/mV, equivalent to Q_x for a synaptic reversal potential 50 mV above V_{rest} .

In the *in vitro* studies, 1.0 to 5.0 second waveforms were scaled by 5 to 20 different values of excitatory synapse synchrony N , set differently for each neuron to span subthreshold, perithreshold, and suprathreshold behaviors. The scaled waveforms for each N were input to each neuron 5 to 20 times as both a conductance and a current. Each neuron received a total of ~ 200 waveform presentations in random order across all N and both modalities, with 5 to 15 s of rest between waveforms. The complete recording duration for each neuron lasted from 20 to 60 min. Data from cells that lived for less than 30 min post-patching were not analyzed.

III. OUTPUT MEAN AND VARIABILITY

Synaptic inputs that are too small to alter substantially either the total membrane conductance or membrane potential are well approximated as time-varying current sources. In this paper, we explore the various ways in which this approximation breaks down in response to physiologically realistic inputs. To begin, we delineate in clear terms the fundamental differences between synaptic inputs modeled as current and conductances. We go on to examine how those differences impact first and second order neuronal output statistics. Finally, we show that conductance inputs enable output reproducibility tuning that is not possible in response to current inputs.

A. Subthreshold responses to current and conductance: Theory and modeling

First, we examine how the synaptic waveform parameters affect the synaptic output statistics. Beginning with the current-based synapses, we can express our model of a synaptic current x as

$$I_x(t) = \frac{Q_x N_x}{\tau_f - \tau_r} \sum_k (e^{-(t-t_{x,k})/\tau_f} - e^{-(t-t_{x,k})/\tau_r}) H(t - t_{x,k}), \quad (5)$$

where x can represent either excitatory or inhibitory currents. Here $H(t)$ is the Heaviside function and the set $\{t_{x,k}\}$ comprises the arrival times of all presynaptic events of type x , characterized by the Poisson rate constant λ_x . The mean value of a Poisson process convolved with a causal, non-negative kernel is the integral from zero to infinity of the kernel times the rate constant. The variance is λ_x times the integral of the squared kernel. For our current-based synapses those relationships yield

$$\langle I_x \rangle = Q_x N_x \lambda_x = Q_x f_x, \quad (6a)$$

$$\sigma_{I_x}^2 = \frac{Q_x^2 N_x^2 \lambda_x}{2(\tau_f + \tau_r)} = \frac{Q_x^2 N_x}{2(\tau_f + \tau_r)} f_x. \quad (6b)$$

The mean synaptic current and the average event rate (f_x) can both be held constant while decreasing (lower N_x , raise λ_x) or increasing (raise N_x , and lower λ_x) the synaptic current variance.

Neurons receive input from excitatory and inhibitory synapses. Applying the previous description to both excitatory (I_e) and inhibitory (I_i) currents, the total synaptic current is $I_{syn}(t) = I_e(t) + I_i(t)$. Near rest Q_e is strictly positive and Q_i strictly negative—for analytic simplicity, we set $Q_0 = Q_e = -Q_i$. Assuming that excitatory and inhibitory signals are independent, the total synaptic mean $\langle I_{syn} \rangle$ and variance $\sigma_{I_{syn}}^2$ are simply the sums of the individual means and variances, respectively,

$$\langle I_{syn} \rangle = Q_0(f_e - f_i), \quad (7a)$$

$$\sigma_{I_{syn}}^2 = \frac{Q_0^2}{2(\tau_f + \tau_r)} (N_e f_e + N_i f_i). \quad (7b)$$

The average synaptic current thus depends on the difference between excitatory and inhibitory synaptic rates, but the syn-

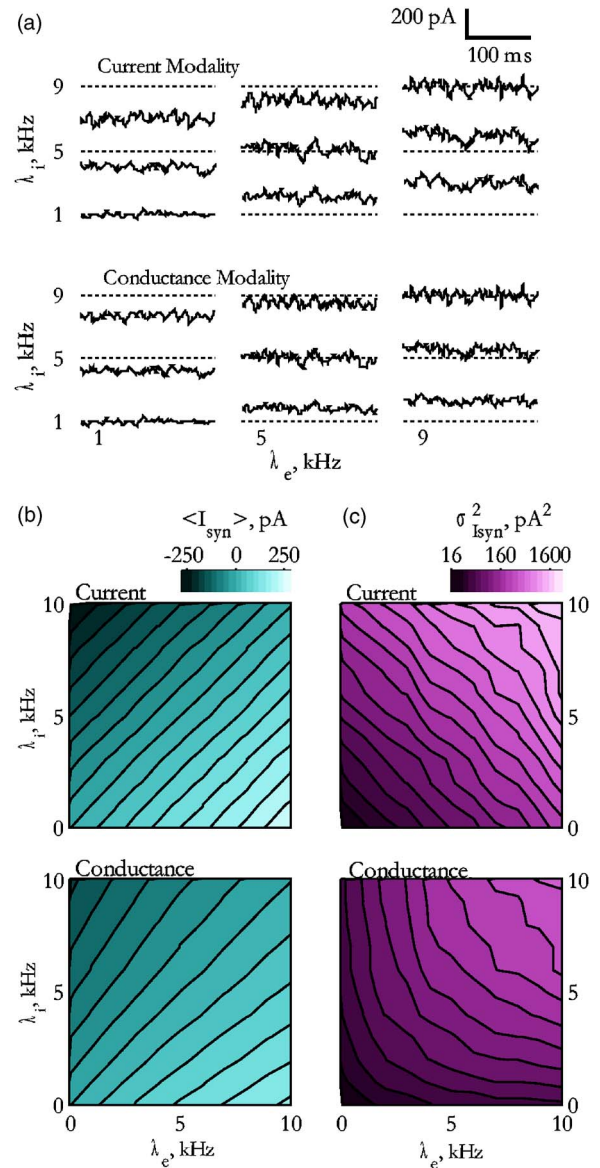


FIG. 3. Synaptic current statistics. Biologically realistic synaptic current to a purely passive neuron. (a) Sample current traces for three values of excitatory (λ_e) and inhibitory (λ_i) synaptic rates, modeled as current-based (top) and conductance-based (bottom) synapses. Dashed lines indicate zero current. (b) Average synaptic current $\langle I_{syn} \rangle$ as a function of λ_e and λ_i . The plots are similar but conductance-based results (bottom) are less parallel than current-based results (top). (c) Synaptic current variance $\sigma_{I_{syn}}^2$ as a function of λ_e and λ_i . Note the logarithmic color scale. The conductance-based simulations (bottom) yielded a differently shaped and largely reduced variance function from the current-based simulations (top).

aptic current variance depends on their sum, weighted by their synchrony. With $N_e = N_i = 1$, lines of constant $\langle I_{syn} \rangle$ are orthogonal to constant $\sigma_{I_{syn}}^2$ in the $\lambda_e - \lambda_i$ plane [Figs. 3(b) and 3(c), top]. While precise orthogonality depends on matching excitatory and inhibitory parameters, the qualitative result does not: $\langle I_{syn} \rangle$ and $\sigma_{I_{syn}}^2$ can be independently tuned by varying $\lambda_e + \lambda_i$ and $\lambda_e - \lambda_i$.

Presenting this synaptic current to the passive membrane of Eq. (4), we can find the membrane potential statistics. Convolution of the membrane potential impulse response with the synaptic kernel, and repeating the procedure used to calculate the current moments above, we find

$$\langle V_m \rangle = \frac{Q_0}{G_m} (f_e - f_i) \quad (8a)$$

$$\sigma_{V_m}^2 = \frac{Q_0^2}{2B_m G_m^2} (N_e f_e + N_i f_i) + \frac{\tau_m}{2} D_m \equiv \sigma_{\langle V \rangle}^2 + \eta_{V_m}^2, \quad (8b)$$

where B_m is simply a time constants scaling factor: $B_m \equiv (\tau_m + \tau_f)(\tau_m + \tau_r)(\tau_f + \tau_r) / (\tau_m \tau_f + \tau_m \tau_r + \tau_f \tau_r)$. We define $\sigma_{\langle V \rangle}^2$ as the variance attributable to the synaptic input current to distinguish it from $\eta_{V_m}^2$, the intrinsic membrane potential variance that by construction is independent of V_m . The notation $\sigma_{\langle V \rangle}^2$ is intended to stress that it is the variance of the average membrane potential waveform $[V_m(t)]$, in response to repeated presentations of the same synaptic input. An inspection of Eqs. (7) and (8) reveals the general result that, shifted by rest potential ($V_{\text{rest}}=0$), the average membrane potential varies proportionally to $\langle I_{\text{syn}} \rangle$. Similarly, in the intrinsic-noise free case ($\eta_{V_m}^2=0$), the membrane potential variance is exactly proportional to $\sigma_{I_{\text{syn}}}^2$. This proportionality holds for many other current modality input models, including white noise²⁶ and certain Ornstein-Uhlenbeck processes.²⁷ The Poisson rates λ_e and λ_i , through their ability to tune out $\langle I_{\text{syn}} \rangle$ and $\sigma_{I_{\text{syn}}}^2$, can be set to achieve any reasonable combination of $\langle V_m \rangle$ and $\sigma_{V_m}^2$.

In the treatment above, we assumed that I_{syn} was equal to the combination of two stationary random process currents, each generated via the sum of many tiny synaptic events. In reality, those synaptic events generate a conductance change across the membrane and are associated with a synaptic reversal potential V_x . It is therefore more realistic to model synaptic currents in the conductance modality:

$$I_x(t) = \frac{\Phi_x [V_x - V_m(t)] N_x}{\tau_f - \tau_r} \sum_k (e^{-(t-t_{x,k})/\tau_f} - e^{-(t-t_{x,k})/\tau_r}) \times H(t - t_{x,k}), \quad (9)$$

where Φ_x is the charge per unit voltage delivered by a single synaptic event. Analogous to Q_0 previous, we set $\Phi_0 = \Phi_e = \Phi_i$. Keeping in mind that we shifted V_{rest} to 0, we correspondingly shift the synaptic reversal potentials and for simplicity set $V_{\text{syn}} = V_e = -V_i$. From Eqs. (4) and (9), the mean total synaptic current and change in average membrane potential are interdependent, and become difficult to derive exactly.

The membrane potential response to a current modality synaptic input is independent of any previous inputs the neuron has received. In the conductance modality, however, the membrane potential response depends on previous inputs. In particular, fluctuations in the synaptic input change not only the membrane potential, but also the effective membrane conductance, both of which affect the response to subsequent inputs. These high order interactions give rise to a skewed membrane potential distribution that has been examined in depth for other synaptic kernels.²⁸ Fortunately, in the limit of a large number of small inputs (large λ , small N) the interaction between the membrane potential deviations and conductance deviations is negligible.²⁹ Making the assumption that this interaction can be neglected yields an analytically

tractable Gaussian-distributed membrane potential. Later, we make this assumption for analytical ease, but explore cases in which it does not hold in the simulations.

Under the Gaussian approximation, the effective average conductance is $G_{\text{eff}} = G_m + \Phi_0(f_e + f_i)$, which yields an effective average time constant: $\tau_{\text{eff}} \equiv C_m / G_{\text{eff}}$. The membrane potential mean follows trivially from the effective conductance, and the variance can be found via the same method employed for the current modality above to yield

$$\langle V_m \rangle \approx \frac{\Phi_0 V_{\text{syn}} (f_e - f_i)}{G_m + \Phi_0 (f_e + f_i)} \equiv \frac{\Phi_0 V_{\text{syn}}}{G_{\text{eff}}} (f_e - f_i), \quad (10a)$$

$$\begin{aligned} \sigma_{V_m}^2 &\approx \frac{(\Phi_0 V_{\text{syn}})^2}{2B_{\text{eff}} G_{\text{eff}}^4} [(G_m + 2\Phi_0 f_i)^2 N_e f_e + (G_m + 2\Phi_0 f_e)^2 N_i f_i] \\ &\quad + \left(\frac{G_m}{G_{\text{eff}}} \right) \frac{\tau_m}{2} D_m \\ &\equiv \frac{(\Phi_0 V_{\text{syn}})^2}{2B_{\text{eff}} G_{\text{eff}}^2} (W_e N_e f_e + W_i N_i f_i) + \frac{\tau_{\text{eff}}}{2} D_m \\ &\equiv \sigma_{\langle V \rangle}^2 + \eta_{V_m}^2, \end{aligned} \quad (10b)$$

where the first forms are written to stress functional dependencies and the second forms are written to stress the parallels with the Eq. (8) current modality results. Similar to Eq. (8), the time constant scaling factor is $B_{\text{eff}} \equiv (\tau_{\text{eff}} + \tau_f)(\tau_{\text{eff}} + \tau_r)(\tau_f + \tau_r) / (\tau_{\text{eff}} \tau_f + \tau_{\text{eff}} \tau_r + \tau_f \tau_r)$. The synaptic scaling factors in the variance are defined as $W_e \equiv [(G_m + 2\Phi_0 f_i) / G_{\text{eff}}]^2$, and $W_i \equiv [(G_m + 2\Phi_0 f_e) / G_{\text{eff}}]^2$. They can be conceptualized as the weight of one synapse type given the average contribution of the other, and approach unity from opposing directions as f_e approaches f_i . Using the same method to find the moments of synaptic current yields

$$\langle I_{\text{syn}} \rangle \approx \frac{G_m \Phi_0 V_{\text{syn}}}{G_{\text{eff}}} (f_e - f_i), \quad (11a)$$

$$\sigma_{I_{\text{syn}}}^2 \approx \frac{(\Phi_0 V_{\text{syn}})^2}{2(\tau_f + \tau_r)} (W_e N_e f_e + W_i N_i f_i). \quad (11b)$$

The average voltages in Eqs. (8a) and (10a) depend on the excitatory-inhibitory frequency difference in both cases, but nonlinearly in Eq. (10a). In the limit that the average input conductance $[\Phi_0(f_e + f_i)]$ is much greater than G_m , the average membrane potential is inversely proportional to the frequency sum. This inverse proportionality is likely the dominant effect *in vivo*, in which experimental recordings show that input conductance can be five times greater than the passive membrane conductance.³⁰ Furthermore, in the conductance modality the larger the total synaptic input gets, the smaller τ_{eff} becomes. From Eq. (10b), we see that as τ_{eff} decreases, the impact of intrinsic membrane potential fluctuations is mitigated. In the current modality in contrast, the effects of intrinsic noise are entirely independent of the input. We will revisit this important distinction later, as it leads to qualitative differences in the relationship between neuronal output variability and reproducibility.

We examined means and variances in passive integrative models. Setting $\Phi_0 = Q_0 / (V_{\text{syn}} - V_{\text{rest}})$, we directly compared

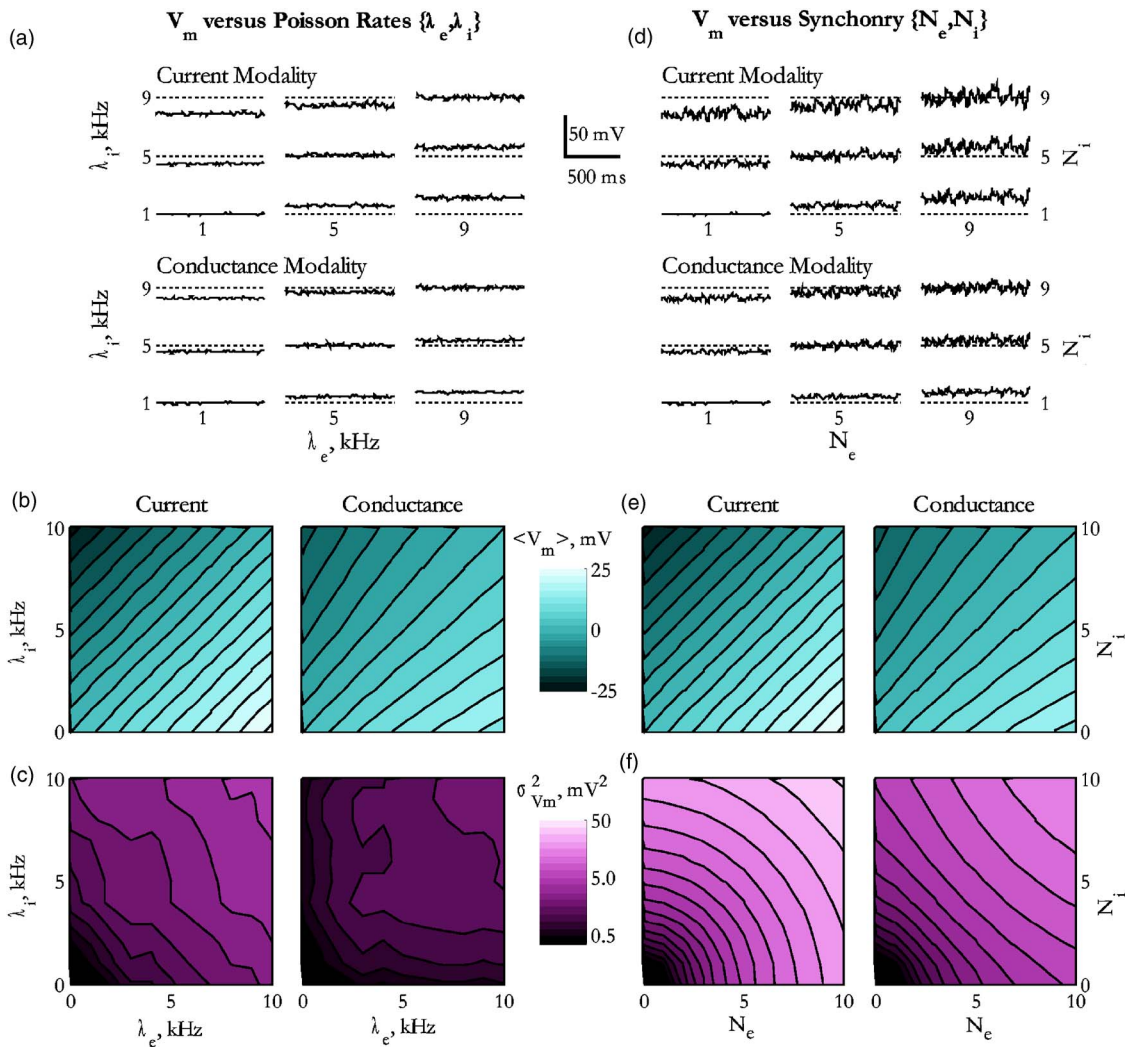


FIG. 4. Membrane potential statistics. Potential of a passive membrane responding to ranging synaptic input waveforms. (a) Sample voltage traces for three values of excitatory (λ_e) and inhibitory (λ_i) Poisson rates (with $N_e=N_i=1$), modeled as current-based (top) and conductance-based (bottom) synapses. Dashed lines indicate the membrane potential rest. (b) Membrane potential means ($\langle V_m \rangle$) as a function of λ_e and λ_i for current (left) and conductance (right) modalities. (c) Membrane potential variances ($\sigma_{V_m}^2$) under the same conditions as b. (d) With (e) and (f), the same format as (a)–(c), but in response to varying excitatory (N_e) and inhibitory (N_i) synaptic synchrony, with $\lambda_e=\lambda_i=1$ kHz. Hence, analogous traces in (a) and (d) are matched for total excitatory ($N_e\lambda_e$) and inhibitory ($N_i\lambda_i$) synaptic inputs. (e) Average membrane potentials are the same as in the fairly matched cases of (b). (f) The potential variances rise much more quickly with N_e and N_i than for λ_e and λ_i , as seen in (c), in both modalities. Note the logarithmic color scale for $\sigma_{V_m}^2$.

the current means and variances generated by the two modalities. Simulations were run for each combination λ_e and λ_i , ranging from 0 to 10 000 Hz in 500 Hz steps (Fig. 3). Synaptic input closely matched theoretical predictions. Synaptic current is less sensitive to λ_e and λ_i when the synapses are modeled as conductances, but the average current is still roughly proportional to the frequency difference [Fig. 3(b)]. However, the current variance in response to conductance-based synapses has a qualitatively different shape than $\sigma_{I_{syn}}^2$ from current-based synapses [Fig. 3(c)]. The conductance-induced variance appears more proportional to the $f_e f_i$ product than to the $f_e + f_i$ sum. This approximately proportional dependence is expected from the dominance of f_i in the W_e term (and f_e in the W_i term) of Eq. (11b).

The most interesting differences between synaptic current and synaptic conductance models are their effects on

neuronal output. From the previous simulations, we also examined the effects on membrane potential [Figs. 4(a)–4(c)]. The average membrane potential ($\langle V_m \rangle$) as a function of λ_e and λ_i behave in the same manner as the synaptic current [Fig. 4(b)]. However, membrane potential variance $\sigma_{V_m}^2$ increases sluggishly with increasing λ_e and λ_i for both modalities [Fig. 4(c)]. This analysis suggests that physiologically realistic, independent synaptic events cannot generate highly variable membrane potential waveforms. Stevens and Zador found similar results *in vitro*.²⁴ They suggested that synchronous synaptic input could be used to generate realistically variable membrane potentials. To explore waveforms more characteristic of synaptic trains *in vivo*, we fixed the Poisson rates to a reasonable minimum value and varied the number of synapses triggered per event: N_e and N_i . Whereas doubling the Poisson rate doubles the number of independent synaptic

events, doubling of the synapses per event doubles the delivered charge.

When all synapses are independent ($N_e=N_i=1$), lumped synaptic current means and variances increase proportionally to each other [via λ_x in Eq. (6)]. When Poisson rates are constant and synaptic synchrony is allowed to vary, lumped synaptic current means increase proportionally to the square root of synaptic current variance [via N_x in Eq. (6)]. Holding, $\lambda_e=\lambda_i=1$ kHz, we repeated the passive membrane simulations as a function of N_e and N_i . By varying these synchrony parameters, the membrane potential variance spans the range observed *in vivo*, without driving the mean potential beyond physiologically realistic limits [Figs. 4(d)–4(f)].

Comparing columns of synaptic conductance modality (Fig. 4), we can summarize three important points. First, by construction, the average membrane potential ($\langle V_m \rangle$) is identically dependent upon $\{\lambda_e, \lambda_i\}$ and $\{N_e, N_i\}$ [Figs. 4(b) and 4(e)]. Second, the potential variance $\sigma_{V_m}^2$ is critically dependent upon $\{N_e, N_i\}$ and relatively unaffected by $\{\lambda_e, \lambda_i\}$ [Figs. 4(c) and 4(f)]. Third, $\langle V_m \rangle$ and $\sigma_{V_m}^2$ are approximately orthogonal in the $\{N_e, N_i\}$ plane. These results generally hold independent of the input modality.

B. Subthreshold responses to current and conductance: Experimental comparisons

Two primary differences between current and conductance-based inputs must be considered. First, conductance inputs reduce the resistance of the postsynaptic membrane, reducing the effectiveness of subsequent inputs. Second, as inputs move the membrane potential nearer to the synaptic reversal potential, the reduction in driving force ($V_{syn}-V_m$) reduces the charge delivered per synapse [$\Phi_0(V_{syn}-V_m)$], independent of the conductance shunt. The contributions of reduced driving force are easily confounded with those of shunting because both decrease the slope of curves in which output statistics, including the membrane potential and firing rate, are plotted against the input strength. A fair comparison between current and conductance would remove the driving force effect, such that the current delivered by the two modalities of pseudosynaptic waveforms could be compared directly. One way to achieve this fair comparison is to plot output statistics versus the total current entering through the synapses.

Because varying synchrony enables realistic levels of potential variance, in our experimental protocol we held the Poisson rate constant ($\lambda=2$ kHz) and ranged the synchrony. To keep our independent variable space one dimensional, we contrasted current and conductance waveforms for excitatory input only, $N_i=0$. Via the dynamic clamp technique, we delivered excitatory input to two classes of superficial entorhinal cortical neurons: stellate and pyramidal neurons. Each pseudosynaptic waveform was delivered 5 to 20 times as both currents and conductances for 5 to 20 values of N_e . Even though N_e was our varying input parameter, we plot output statistics versus the average synaptic current ($\langle I_{syn} \rangle$), calculated post hoc for each waveform, to isolate the shunting effects (Fig. 5).

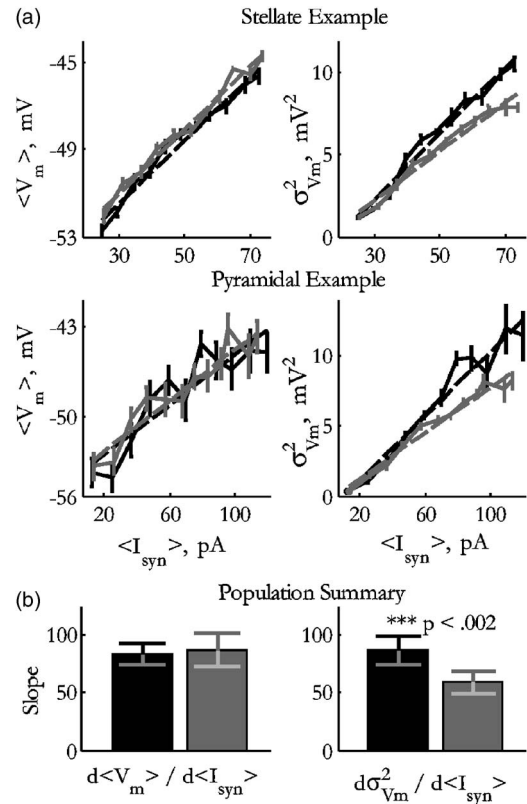


FIG. 5. Conductance input mitigates $\sigma_{V_m}^2$ increases. Membrane potential means ($\langle V_m \rangle$, left) and variances ($\sigma_{V_m}^2$, right) as a function of the average applied current ($\langle I_{syn} \rangle$). (a) Potential statistics in an example stellate (top) and pyramidal (bottom) neuron, in response to the pseudosynaptic current (black) and conductance (gray). Error bars denote s.e.m. over the number of trials repeated at each stimulus amplitude. Dotted lines indicate a least-squared linear fit. Variance increases more slowly as a function of $\langle I_{syn} \rangle$ for conductance-based inputs. (b) Slopes of the above curves averaged over 14 neurons for which a minimum of three subthreshold input amplitudes were examined. While $\langle V_m \rangle$ was not affected by input modality, $\sigma_{V_m}^2$ increased more slowly in response to increasing pseudosynaptic conductance. Indicated p values from the paired T test.

When plotted versus $\langle I_{syn} \rangle$, the average membrane potential ($\langle V_m \rangle$) was not affected by the input modality (Fig. 5, left). In other words, the average shunting effect of a synaptic input was not felt by the input itself. This underappreciated fact can be understood by solving for the average input conductance. Dividing $\langle I_{syn} \rangle$ from Eq. (11a) by $\langle V_m \rangle$ from Eq. (10a) yields exactly G_m , independent of all other factors. To verify this result experimentally, we calculated a linear least-squared fit to the $\langle V_m \rangle$ versus $\langle I_{syn} \rangle$ curves for all neurons. The slope R_m of this fit does not differ between modalities [Fig. 5(b), left].

The membrane potential variance $\sigma_{V_m}^2$ was smaller in response to the conductance modality input (Fig. 5, right). We performed a linear least-squared fit to the $\sigma_{V_m}^2$ versus $\langle I_{syn} \rangle$ curves for the same neurons. The slope estimates from $\sigma_{V_m}^2$ in the conductance modality are consistently and substantially less than in the current modality [Fig. 5(b), right]. The response to input variance depends on the input mean: the more average input conductance, the less variable the

output becomes.³¹ In summary, while $\langle V_m \rangle$ is only a function of the average synaptic current, σV_m^2 depends on the conductance as well.

C. Suprathreshold responses to current and conductance: $f-I$

Neuronal firing frequency versus applied current functions, so called $f-I$ curves, are easily measured from neurons *in vitro*. In general, the slope of the $f-I$ curve decreases with decreasing membrane resistance. To demonstrate this point, $f-I$ curves can be measured in the presence of synaptic background activity. With different computational models of the pseudosynaptic background, it has been shown that increasing the difference between the excitatory and inhibitory conductances shifts the $f-I$ curve, while increasing their sum changes the slope of the curve.³² Dynamic clamp studies have confirmed this result by demonstrating that $f-I$ curve slopes, measured as a function of some constant applied current, decrease with increasing synaptic activity.¹⁶ As such, the background activity is said to shunt the neuronal membrane. In the *in vivo* condition, however, there exists no constant applied current. All inputs arrive as synaptic events—there is no distinction between synaptic signals and synaptic background. To properly examine to what extent activity is shunting neuronal input, we eliminate the artificial distinction between signal and background and isolate shunting effects by accounting for charge mitigation.

We simulated an integrate-and-fire model for both input modalities, ranging N_e from 1.0 to 7.0 in steps of 0.25 and N_i from 0.0 to 4.0 in steps of 0.50 (Fig. 6). Plotted as a function of N_e , the curves shifted right and decreased in slope for increasing N_i in both modalities [Fig. 6(b)], indicative of N_i induced decreases in average membrane potential. The same data plotted against the synaptic current nearly overlies, however, particularly at higher firing rates [Fig. 6(c)]. Close inspection [Fig. 6(c), inset] reveals that slope changes at low firing rates with changes in N_i . In this perithreshold regime, characterized by long and variable interspike intervals, Shadlen and Newsome showed that the firing rate is controlled by membrane potential fluctuations.² Since variance increases with N_e and N_i (Fig. 4), the perithreshold firing rate is modulated through synchrony-induced membrane potential fluctuations. This firing rate modulation in the perithreshold regime is an example of noise-induced softening of a static nonlinearity, which can decrease the phase lag of neuronal responses to high frequency input.³³

Borg-Graham and colleagues suggested that *in vivo* shunting effects may limit the ability of potential fluctuations to control the firing rate in the excitable regime.³⁴ Indeed, differences between the curves of different N_i are smaller in the conductance modality [Fig. 6(c), inset]. However, comparing N_i -matched lines across modalities near the threshold, conductance-based inputs are right-shifted with respect to current-based inputs, particularly for larger values of N_i . This right-shift corresponds to excess conductance mitigating the noise-induced threshold softening. This right-shift and the correspondingly increased slope (required to asymptote to the same curve) are the only functional effects of shunting.

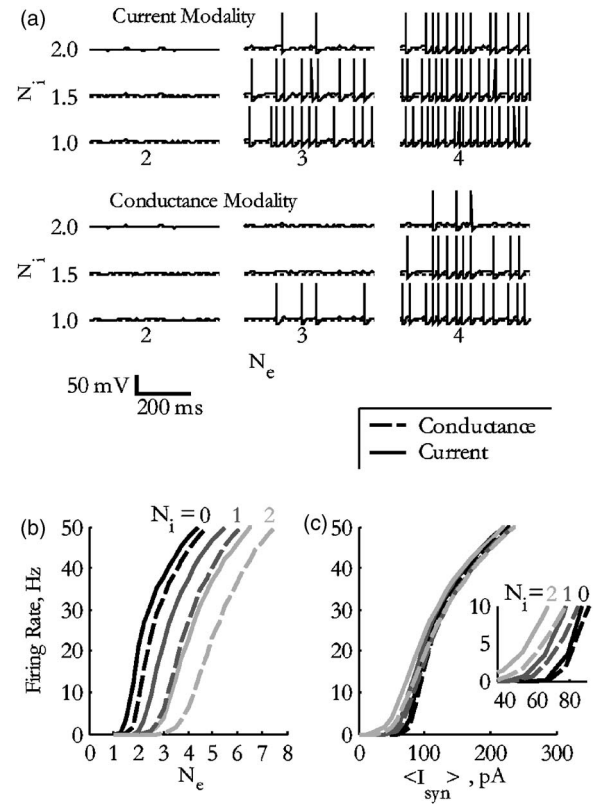


FIG. 6. Firing rate versus synaptic synchrony. The effects of synchronous synaptic activity on firing rate in an integrate-and-fire model. (a) Sample voltage traces for three values of excitatory (N_e) and inhibitory (N_i) strength, where the synaptic strength is the number of synapses that fire synchronously per synaptic event. Synapses are current-based (top) and conductance-based (bottom) models. Dashed lines indicate membrane potential rest. (b) The average firing rate as a function of N_e for current- (solid) and conductance- (dashed) based inputs, for three values of N_i : {0, 1, 2} from left to right. (c) The same data as in (b), only plotted against the average current flowing through the synaptic input. All lines approach the same asymptote. Close inspection (inset) reveals that for a given N_i , current-based inputs near the threshold induce higher firing rates than conductance-based inputs.

As with membrane potential variance, the primary difference between current- and conductance-based inputs is in the output variability. We verified this effect experimentally by examining firing rates in response to pseudosynaptic input from both modalities via the dynamic clamp (Fig. 7). As in Fig. 6, plotting the firing rate versus N_e revealed a graph that superficially appears to include a membrane potential shunt effect [Fig. 7(a)]. However, once corrected for the driving force by plotting versus $\langle I_{syn} \rangle$, the only remaining difference is in the excitable regime near the threshold [Fig. 7(b)]. We verified this difference across the population of 14 neurons by measuring the current threshold for action potential initiation in both modalities. The threshold for conductance input was higher than for the current input ($p < 0.01$ in the pairwise T test) by 8.6 ± 2.4 pA (mean \pm sem).

In the model, we examined variability versus the firing rate for a range of conditions. (Because this examination requires a large set of stationary data, it was not possible to perform for experimental data.) For a fixed firing rate, the coefficient of variation of membrane potential ($CV_{V_m} = \sigma_{V_m} / \langle V_m \rangle$) and the interspike interval (isi) coefficient of

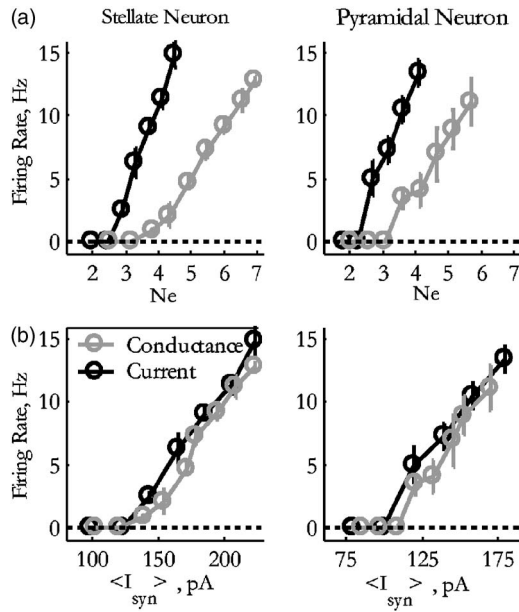


FIG. 7. Conductance input only affects threshold. Action potential threshold and firing rate as a function of synaptic current in stellate (left) and pyramidal (right) neurons. (a) The average firing rate as a function of synaptic strength (N_e) in response to pseudosynaptic current (black) and conductance (gray) in a typical cell from each class. Error bars denote the standard deviation over the number of trials repeated at each stimulus amplitude. (b) The average firing rate as a function of the average synaptic current $\langle I_{syn} \rangle$. The only remaining difference is at low firing rates near the threshold.

variation ($CV_{isi} = \sigma_{isi} / \langle isi \rangle$) are both consistently higher for increasing values of N_i (Fig. 8). By tuning N_e and N_i , a range of spike time variabilities can be achieved for any firing rate [Fig. 8(b)].

IV. NEURONAL REPRODUCIBILITY

The previous results show that in charge-balanced situations, the membrane potential variance is decreased by conductance and the action potential threshold is increased. In this section, we turn our attention away from simple statistics to address the differences in neuronal output reproducibility as a function of the input. In response to identical suprathreshold inputs, the output of a neuron converges to some theoretical ideal waveform $\tilde{V}_m(t)$, determined by the inputs and the neuron itself.^{35,36} In the most general context, we consider reproducibility as the similarity of a neuron’s actual response to $\tilde{V}_m(t)$. We measure reproducibility via separate statistics in the sub- and suprathreshold regimes.

A. Subthreshold reproducibility: Signal-to-noise ratio

To examine subthreshold reproducibility, we simulated a passive integration model with an additive noise term for both input modalities (Fig. 9). Again holding $\lambda_e = \lambda_i = 2$ kHz, we ranged N_e and N_i . For each parameter set, we ran the model without a noise source to establish the membrane potential trajectory in the absence of noise, $\tilde{V}_m(t)$. The signal strength was found as the variance of the ideal trajectory and labeled $\sigma_{(V)}^2$ from Eqs. (8b) and (10b), where the notation reminds us that $\langle V_m(t) \rangle$ is an estimate of $\tilde{V}_m(t)$. We ran each model with exactly the same synaptic inputs 32 more times for different additive noise realizations. The noise variance $\eta_{V_m}^2$ was calculated as the average squared difference between realizations $V_m(t)$ and ideal trajectory $\tilde{V}_m(t)$. Since they are independent—precisely in the current modality, approximately in the conductance modality—they sum to the potential variance: $\sigma_{V_m}^2 = \sigma_{(V)}^2 + \eta_{V_m}^2$.

Signal strength $\sigma_{(V)}^2$ increased with input synchrony in both modalities, but the effect was particularly strong in response to current inputs [Fig. 9(b)]. As expected from Eqs. (8b) and (10b), noise variance $\eta_{V_m}^2$ was constant in the current modality, but decreased dramatically with increasing N_e and N_i in the conductance modality [Fig. 9(c)]. The signal-to-noise ratio was found as $\rho_{V_m} = \sigma_{(V)}^2 / \eta_{V_m}^2$. Comparing ρ_{V_m} across modalities, the current-induced $\sigma_{(V)}^2$ increase and the conductance-induced $\eta_{V_m}^2$ decrease largely cancel each other out, leaving signal-to-noise ratios largely independent of modality, excluding very large $\langle I_{syn} \rangle$ [Fig. 9(d)].

In living neurons, noise sources are not simply additive. We examined the role that increasing conductance plays in the presence of more realistic noise sources *in vitro* (Fig. 10). Because our protocol did not keep the average membrane potential constant, we again account for the driving force by plotting the data versus the average applied current, which increased with N_e , in both modalities. The ideal trajectory $\tilde{V}_m(t)$ was estimated as the average $\langle V_m(t) \rangle$ across all trials. As in the model, signal strength $\sigma_{(V)}^2$ was higher for current-

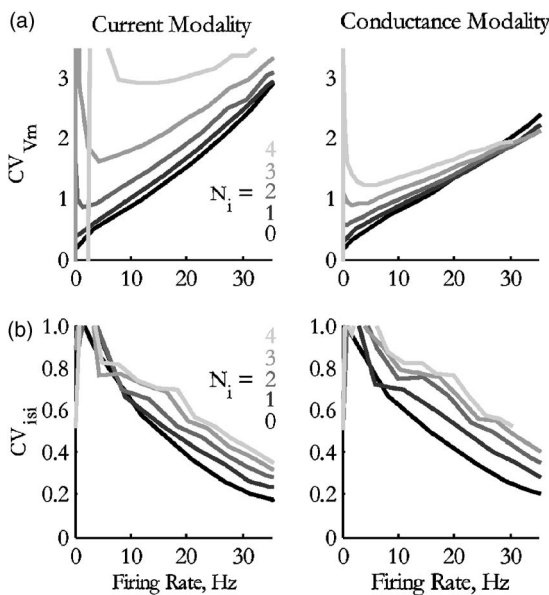


FIG. 8. Synaptic synchrony increases spike time variability. The effects of current- (left) and conductance- (right) based synchronous synaptic activity on membrane variability in an integrate-and-fire model. Data from same trials as in Fig. 6. (a) Potential coefficient of variation ($CV_{V_m} = \sigma_{V_m} / \langle V_m \rangle$) as a function of the firing rate for five values of N_i : {0, 1, 2, 3, 4} from bottom to top. (b) The interspike interval coefficient of variation ($CV_{isi} = \sigma_{isi} / \langle isi \rangle$) as a function of the firing rate. For a given firing rate, variability increases with synaptic synchrony.

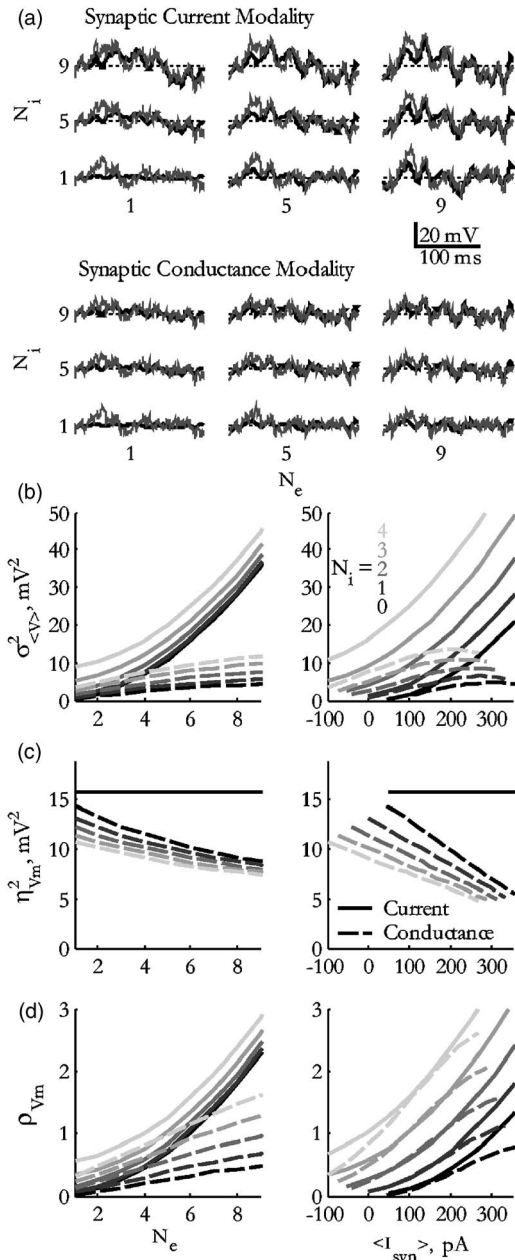


FIG. 9. Signal-to-noise ratio. The relationship between membrane potential ideal trajectory variance $\sigma_{\langle V \rangle}^2$ and noise variance $\eta_{V_m}^2$ in an integrate-and-fire neuron with an intrinsic additive noise term, for varying values of excitatory (N_e) and inhibitory (N_i) synaptic synchrony, with $\lambda_e = \lambda_i = 2$ kHz. (a) Sample voltage traces of the ideal trajectories ($D_m = 0$; black lines) and in the presence of an intrinsic noise term [$D_m = 2(4 \text{ mV})^2 / \tau_m$; gray lines] for three values of N_e and N_i , in response to the pseudosynaptic current (top) and conductance (bottom) inputs. (b) With (c) and (d), the same data are plotted versus two measures of excitatory input strength, N_e (left) and average current $\langle I_{\text{syn}} \rangle$ (right), for five values of N_i as labeled. The ideal trajectory variance $\sigma_{\langle V \rangle}^2$ increases with excitatory input strength and N_i , but increases much more quickly in the current modality. (c) The noise variance $\eta_{V_m}^2$ is constant (all five lines overlay) in the current modality, but decreases with excitatory input strength and N_i in the conductance modality. (d) Signal-to-noise ratio found as data in (b), divided by data in (c).

based inputs [Fig. 10(a)]. Noise variance $\eta_{V_m}^2$ was consistently lower for evenly matched conductance inputs [Fig. 10(b)].

To quantify the change in reproducibility for our *in vitro* data, we calculated the signal-to-noise ratio ρ_{V_m} for each

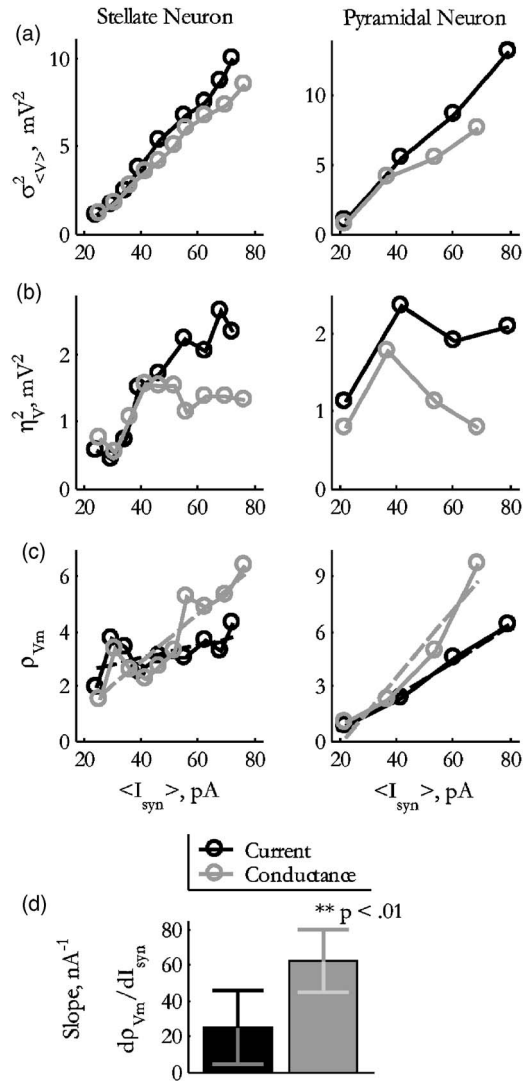


FIG. 10. Signal-to-noise ratio increases with conductance. The relationship between the membrane potential ideal trajectory variance $\sigma_{\langle V \rangle}^2$ and noise variance $\eta_{V_m}^2$ in stellate (left) and pyramidal (right) neurons in the current (black) and conductance (gray) modalities. (a) Example $\sigma_{\langle V \rangle}^2$ found as the variance of the average membrane potential trajectory across trials for two typical cells. Here $\sigma_{\langle V \rangle}^2$ increases more quickly in the current modality. (b) Example $\eta_{V_m}^2$, found as the average squared difference between each trial and the average trajectory. Current-modality $\eta_{V_m}^2$ is increasingly larger than conductance-modality $\eta_{V_m}^2$ for increasing $\langle I_{\text{syn}} \rangle$. (c) The signal-to-noise ratio ρ_{V_m} , found as data in (a), divided by data in (b). Linear fits were made to these curves for all cells (dotted lines). (d) Slopes of the linear fits in (c) averaged over 14 neurons. The twofold difference in average slopes of the ρ_{V_m} vs $\langle I_{\text{syn}} \rangle$ fits ($d\rho_{V_m}/dI_{\text{syn}}$) indicate that increasing conductance is an efficient way of increasing ρ_{V_m} . Statistical p values calculated from the matched-pair Wilcoxon test.

value of $\langle I_{\text{syn}} \rangle$ in both modalities. The signal-to-noise ratio increased with $\langle I_{\text{syn}} \rangle$ because $\sigma_{\langle V \rangle}^2$ nearly always increased faster than $\eta_{V_m}^2$. However, a linear fit to the ρ_{V_m} versus $\langle I_{\text{syn}} \rangle$ curve is typically twice as steep for the conductance modality than for the current modality [Fig. 10(d)]. Hence the signal-to-noise ratio increases more quickly when total conductance increases with an applied current. This finding could not be reproduced in the integrate-and-fire model, suggesting that it is a consequence of the nonlinear membrane

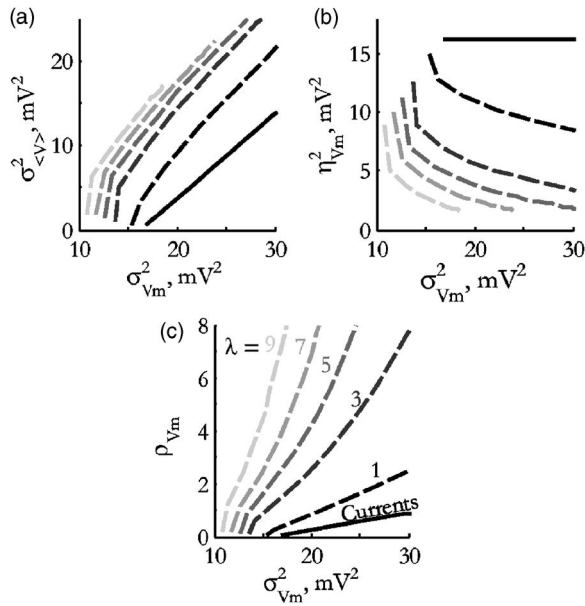


FIG. 11. Conductance enables signal-to-noise tuning. Relationship between membrane potential ideal trajectory variance $\sigma_{\langle V \rangle}^2$ and noise variance $\eta_{V_m}^2$ in an integrate-and-fire neuron with an intrinsic additive noise term. Excitatory and inhibitory Poisson rates were made equal to each other ($\lambda_e = \lambda_i = \lambda$) and varied over the five values indicated. To hold the average membrane potential at rest, N_e and N_i were also made equal, and ranged to vary $\sigma_{V_m}^2$. (a) Ideal trajectory variance $\sigma_{\langle V \rangle}^2$ as a function of $\sigma_{V_m}^2$ for constant $\langle V_m \rangle$. Higher Poisson rates increase the trajectory variance in the conductance modality (dashed lines), but have zero effect in the current modality (solid lines: all five lines precisely overlay). (b) Noise variance $\eta_{V_m}^2$ decreases with increasing λ in the conductance modality, but has zero effect in the current modality (all five lines precisely overlay). (c) In the current modality, ρ_{V_m} and $\sigma_{V_m}^2$ are linearly related and independent of λ . In the conductance modality, for any value of $\sigma_{V_m}^2$, the signal-to-noise ratio ρ_{V_m} can vary over a wide range as a function of λ .

conductances and/or their voltage-dependent intrinsic noise contributions.

Under our increasing N_e paradigm, the model ρ_{V_m} is independent of modality, whereas the *in vitro* data ρ_{V_m} is higher for conductance-based inputs. This interesting difference lead us to further explore conductance induced signal-to-noise changes in the model. We fixed the average membrane potential to rest by setting $N_e = N_i \equiv N$ and $\lambda_e = \lambda_i \equiv \lambda$. We ranged λ from 1 to 9 kHz and varied N upward from 0. Recall from Eqs. (8) and (10) that while both parameters affect the membrane potential mean, N has a dominant effect on variance (Fig. 4). Every simulation for Fig. 11 has the same average membrane potential. Hence, each vertical slice through the plots of Fig. 11 corresponds to a line of constant $\sigma_{V_m}^2$ and $\langle V_m \rangle$.

Increasing λ increases the signal strength in the conductance modality, but has zero effect in the current modality [Fig. 11(a)]. Increasing λ decreases noise strength in the conductance modality, but has zero effect in the current modality [Fig. 11(b)]. For fixed $\sigma_{V_m}^2$ and $\langle V_m \rangle$, the current modality ρ_{V_m} is determined, regardless of N or λ [Fig. 11(c)]. However, the signal-to-noise increases with λ in the conductance modality [Fig. 11(c)]. In the current modality, ρ_{V_m} is exactly defined by the variance, and the neuronal output space is two dimensional: $\langle V_m \rangle$ and $\sigma_{V_m}^2$. In the conductance modality,

ρ_{V_m} is an additional independent dimension that synaptic input can tune. Thus, the conductance modality enables tuning of reproducibility, whereas the current modality does not.

B. Suprathreshold reproducibility: Spike-time reliability

To quantify the reproducibility suprathreshold, we turn to the notion of reliability.³⁷ Identical suprathreshold stimuli were presented repeatedly to neurons at several amplitudes in both modalities. Desired spikes, induced from the synaptic signal as opposed to intrinsic noise sources, were identified via separate algorithms for computational and *in vitro* neurons, as described later. Both algorithms yielded K_{ideal} spike times. Each trial had its own number of spikes, K_{trial} . Reliable spikes were defined as those occurring within σ_τ of a desired spike time; K_{rely} = number of reliable spikes in a trial. The presented data were calculated with $\sigma_\tau = 4$ ms, but values from 1.5 to 15 ms yielded qualitatively similar results. Each trial was given a reliability score, Ψ_{trial} , as the number of reliable spikes divided by the average number of spikes, $\Psi_{\text{trial}} = K_{\text{rely}} / [(K_{\text{trial}} + K_{\text{ideal}}) / 2]$. The reliability scores from all trials for an input were averaged to yield the total reliability $\Psi_{\%}$ for that input, ranging from 1.0 for perfectly reliable to 0.0 for perfectly unreliable.

For computational experiments, we began by holding $\lambda_e = \lambda_i = 2$ kHz, ranged N_i from 0 to 4, and increased N_e , as necessary to achieve different output firing rates. As before, we used identical random number series to generate the excitatory and inhibitory synaptic waveforms for each amplitude. We ran a simulation for each waveform without an intrinsic noise source, $D_m = 0$. All spikes in this noise-free trial were defined as desired spikes. Simulations were repeated with the same synaptic input, but 32 different realizations of a realistically low amplitude intrinsic noise source, $D_m = 2(1 \text{ mV})^2 / \tau_m$. Reliability for each amplitude was calculated from the desired spike times as described previously [Fig. 12(a)]. Reliability increases with $\langle I_{\text{syn}} \rangle$ and N_i [Fig. 12(b)]. Although slightly higher in the conductance modality, reliability as a function of firing rate was primarily independent of input modality [Fig. 12(c)].

For the *in vitro* experiments, identical pseudosynaptic waveforms were presented as current or conductance, scaled by a ranging N_e . For each input amplitude, all elicited spike times were combined to form a series of discrete unit-amplitude delta functions that was convolved with a unit-amplitude Gaussian window, parametrized by standard deviation σ_τ . The waveform amplitude was divided by the number of repeated trials, yielding a smooth spike-time probability function. Desired spike times were defined as local maxima in the probability function that exceeded 0.5. Reliability was calculated as described previously and plotted versus the neuronal firing rate (Fig. 13). In both modalities, $\Psi_{\%}$ increased with the firing rate, consistent with increasingly synchronous input. In pyramidal neurons, $\Psi_{\%}$ as a function of the neuronal firing rate was typically higher in the conductance modality [Figs. 13(b) and 13(c), right]. In stellate neurons the results were not as clean, although a $\Psi_{\%}$ peak was consistently present in the conductance modality at the neuron's preferred firing rate, f_θ [Fig. 13(b), left]. From

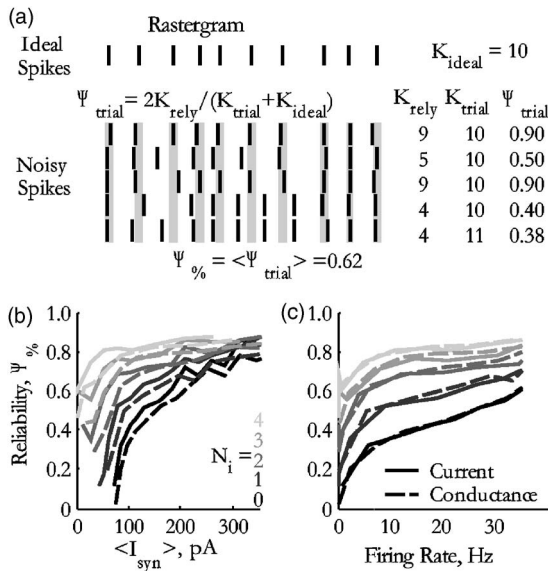


FIG. 12. Model spike-time reliability. Spike-time reliability $\Psi_{\%}$ in an integrate-and-fire neuron with an intrinsic additive noise term. (a) Rastergram of spike times of a model neuron in response to repeated presentations of the same pseudosynaptic input. The top row depicts K_{ideal} spike times, identified by running the model with no intrinsic noise term ($D_m=0$). The other rows depict K_{trial} spike times from five repetitions with different realizations of an intrinsic noise term [$D_m=2(1 \text{ mV})^2/\tau_m$]. Spikes that occurred within the gray bars, corresponding to the ideal spike time with which they align, were counted as reliable, and summed to yield K_{rely} . (b) The procedure in (a) was repeated in both modalities for increasing N_e and five levels of N_i , as indicated. Reliability increased with total synaptic current and N_i , and was higher for current inputs than for conductance inputs at a given value of $\langle I_{syn} \rangle$. (c) Plotted against the output firing rate, $\Psi_{\%}$ increased with N_i . The conductance modality yielded a small but consistent reliability increase over the current modality at a given value of the firing rate.

population data over the stellate neurons examined, conductance increased reliability at f_{θ} ($p < 0.01$, two-tailed, pairwise T test) and its first harmonic ($2f_{\theta}$) and subharmonic ($f_{\theta}/2$), but the effect was small [Fig. 13(c), left].

To better understand the relationship between input modalities, reliability and variability, we performed one final computational experiment to control for the mean output. As we had for the signal-to-noise ratio simulations (Fig. 11), we set $\lambda_e = \lambda_i = \lambda$, and ranged λ from 1 to 9 kHz. For each value of λ , we ranged N_e from 1 to 13. For each parameter pair $\{\lambda, N_e\}$, we found the N_i that yielded an average output firing rate of 20 ± 0.2 Hz over 180 s of simulation time. (For low values of λ and N_e , no non-negative value of N_i could yield a firing rate of at least 20 Hz. Stimulation waveforms that could not yield a 20 Hz firing rate were not considered.)

Reliability was calculated as previously, from 32 realizations of a realistically low amplitude intrinsic noise source, $D_m=2(1 \text{ mV})^2/\tau_m$. Since all synaptic waveforms yielded the same average firing rate, we plot $\Psi_{\%}$ against the interspike interval coefficient of variation (CV_{isi}), a measure of output variability (Fig. 14). Hence, each vertical slice through Fig. 14 corresponds to a line of constant firing rate and CV_{isi} . In the current modality, $\Psi_{\%}$ is completely defined by CV_{isi} , independent of λ or N . As was true in the subthreshold case, the suprathreshold output space is two dimensional: the firing rate by variability. In the conductance modality, however, increasing values of λ right-shift the $\Psi_{\%} - CV_{isi}$ curves. Re-

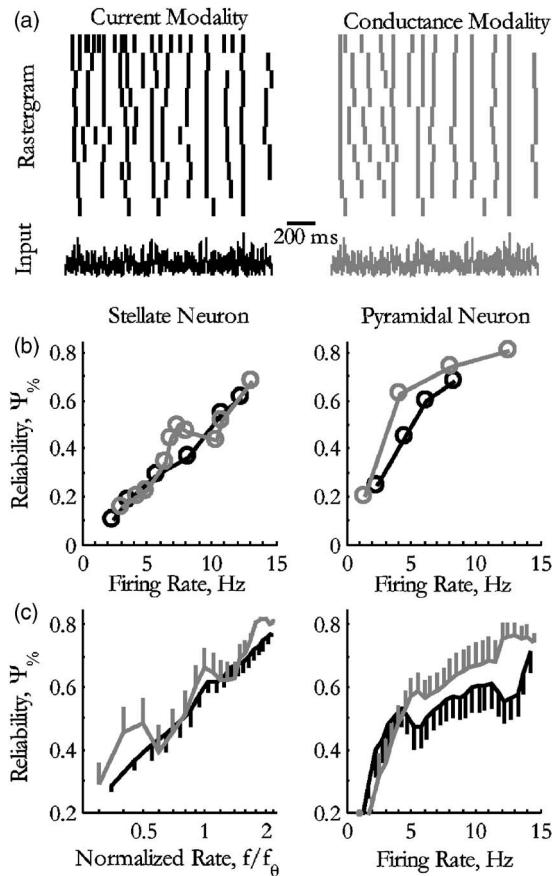


FIG. 13. Spike-time reliability increases with conductance. Repeated presentations of identical pseudosynaptic trials yielded highly reliable spike times. (a) Spike-time rastergrams of a stellate neuron in response to identical waveforms (bottom) presented in both the current (left) and conductance modality (right). A reliability $\Psi_{\%}$ was calculated for each input amplitude, as described in the text. (b) Reliability as a function of the average firing rate in response to conductance (gray) and current (black) for an example stellate (left) and pyramidal (right) neuron. (c) Reliability with standard error measures from population data of eight stellate and six pyramidal neurons. Stellate neuron $\Psi_{\%}$ is plotted against the firing rate normalized by the preferred firing rate f_{θ} , defined as the frequency of their maximum reliability in the theta frequency range (4 to 12 Hz).

liability is a third dimension in the suprathreshold output space, tunable by adjusting the relative contributions of the Poisson rates and synchrony strengths. While the right-shift looks different from the experimental left-shifts of Fig. 13, those data are plotted versus the firing rate only. It is not feasible to control for the firing rate and variability *in vitro*.

V. DISCUSSION

A. Current versus conductance

Several differences distinguish current- from conductance- induced behavior. First, more excitatory synaptic inputs are required to reach a given level of depolarization in response to realistic synaptic conductances than in a current input model. This result is primarily mediated through the driving force. As the membrane potential becomes increasingly positive, the effective charge that flows through each additional excitatory synapse diminishes (Figs. 3 and 4). When comparing neuronal activity in response to the two

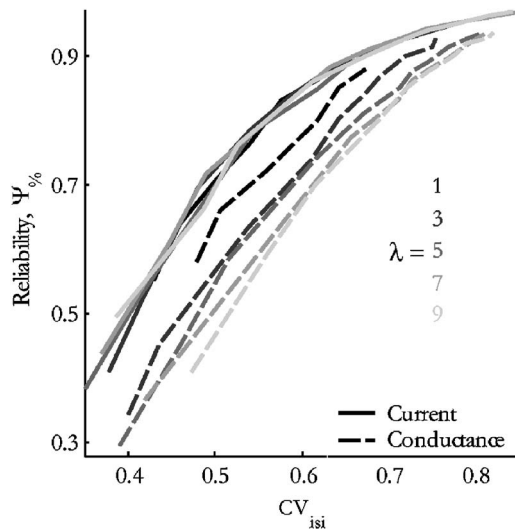


FIG. 14. Conductance enables reliability tuning. The relationship between spike-time variability CV_{isi} and reliability $\Psi_{\%}$ for an integrate-and-fire neuron with an intrinsic additive noise term [$D_m = 2(1 \text{ mV})^2/\tau_m$], in response to current (solid lines) and conductance (dashed lines) modality input. Excitatory and inhibitory Poisson rates were made equal to each other ($\lambda_e = \lambda_i \equiv \lambda$) and varied over the five values indicated. For each λ , N_e was ranged from 1 to 13. For each pair $\{\lambda, N_e\}$, N_i was adjusted to yield a neuronal firing rate of 20 Hz. Trials consisted of 180 s of simulation time, and were repeated with 32 different realizations of intrinsic noise, for each parameter set $\{\lambda, N_e, N_i\}$. In the current modality for fixed frequency, all lines of constant λ overlay in the CV_{isi} by $\Psi_{\%}$ plane. In the conductance modality, increasing the Poisson rates produces a rightward shift in the curves.

modalities, this driving force effect is easily accounted for by considering membrane potential statistics as a function of the total synaptic current (Figs. 5–7).

The second difference between current and conductance is both more subtle and, we believe, more important. With increasing conductance, output variability is reduced even after accounting for the driving force: the membrane potential variance is lower (Figs. 4 and 5); noise-induced threshold softening is weakened (Figs. 6 and 7); and the effective amplitudes of intrinsic noise sources are diminished (Figs. 9–11).

The most important difference between current and conductance inputs is that conductance enables reproducibility tuning. In both sub- and superthreshold regimes in response to current input, reproducibility reflects variability (Figs. 11 and 14, solid lines). In response to realistic conductance waveforms, however, the statistics of the input can tune both the signal-to-noise ratio and reliability, independent of membrane variance and spike time variability, respectively (Figs. 11 and 14, dashed lines).

This phenomenon of increased reliability in the conductance modality may be amplified by differential effects of current versus conductance inputs on membrane potential means and variabilities. The increased conductance may alter reliability through changes in neuronal resonance.³⁸ Perhaps the reliability peak observed in stellate cells (Fig. 13) was not seen in the model because the small amount of resonance exhibited by integrate-and-fire neurons is abolished by modest noise.³⁹ Furthermore, for a given firing rate and interspike interval variability, the membrane potential can be substan-

tially higher in response to conductance-based inputs (Figs. 6–8). The change in the average membrane potential will impact the average state of voltage dependent ion channels, which may also impact reliability.⁴⁰

B. Presynaptic input parameter tuning

The relative effects of current and conductance-based inputs aside, what have we learned about synaptic waveforms? We modeled our pseudosynaptic input as a Poisson train convolved with a difference-of-exponentials synapse function. The Poisson nature gives the stimulus a Gaussian noise characteristic, colored by the time constants of the synapse function. An important assumption that we made was to consider all presynaptic events as uncorrelated, and their total activity occurring with a characteristic rate λ . To impose a degree of order upon those uncorrelated events, we scaled all synaptic events by a synchrony parameter N . Hence, the total rate of presynaptic activity is the product, $f = N\lambda$.

Other parameters of our model were artificially matched, simplifying our analysis. For example, we assumed that excitation and inhibition had identical time constants. Because these time constants are not identical in biological systems, our data figures are more symmetrical than one would otherwise expect, but that symmetry is irrelevant to a qualitative interpretation of our results. Furthermore, some parameters that we held constant could be varied to yield similar effects to those we explored. For example, from a simple inspection of Eqs. (5)–(8), ranging Q_e and Q_i would have the same effects as ranging N_e and N_i . However, most synaptic parameters, including Q_e and Q_i , do not vary over short time scales. On the other hand, the number of synchronous presynaptic events is often greater than one (many presynaptic neurons impact their postsynaptic targets with multiple synapses) and may very well be modified by behavioral states. For example, the degree of synchronous activity in the hippocampus is greatly increased during the so-called theta rhythm, expressed during periods of active exploration. Imagine two otherwise uncorrelated hippocampal pyramidal cells fire synchronously during the theta rhythm. If both cells synapse onto the same downstream neuron, that neuron will experience an effective increase in N during active exploration. If both presynaptic neurons continue to fire at the same average rate, then in our construction λ will be reduced such that f is left unaffected.

In this paper, we have shown that presynaptic inputs can set any membrane potential or firing rate over a wide range of input parameter values, enabling fine tuning of output variability. Membrane potential variance is roughly orthogonal to the mean membrane potential in the $N_e - N_i$ plane (Fig. 4). At a fixed average membrane potential, noise variance decreases with increasing conductance, from either N or λ [Fig. 11(b)]. The membrane potential variability and interspike interval variability increase with N_e and N_i for any given firing rate (Fig. 8).

Spike-time variability closely parallels reliability (Fig. 14). This finding confirms *in vivo* results that highly variable neuronal outputs are highly reproducible across trials⁴¹ and computational results that neuronal information is more correlated with input variability (i.e., N_e and N_i) than with the

average output firing rate.⁴² However, like most reliability measures, ours relies on the existence of a single ideal response, and that noise-induced shifts from that ideal may alter single spike times, but will not change the trajectory. While this perspective reflects reality for small noise sources and very long duration stimuli,³³ it may be oversimplified for short trials. In particular, for brief duration inputs, multiple ideal trajectories may exist. The output of a neuron may depend on the neuronal initial state when the input begins, and may jump between trajectories given the right realization of intrinsic noise.⁴³ Nonetheless, highly variable spike trains are not necessarily highly reliable. Finely tuned input can vary reliability without changing the interspike interval variability.⁴⁴ Additionally, our review has focused only on synaptic waveforms without any long-term correlations. Other work has shown that long, temporal correlations in synaptic input (e.g., $\tau_f > 20$ ms) can drastically reduce spike-time reliability.¹⁰

In response to physiologically realistic conductance-based inputs, we propose that neuronal responses span an output space that includes average rate, variability of rate, and reproducibility. The average value of an output (membrane potential or firing rate) is set by the difference in average charge flow between excitatory and inhibitory synaptic signals, $\lambda_e N_e - \lambda_i N_i$ in our case of matched amplitudes, time constants, and synaptic potentials. The output variability (potential variance or interspike interval coefficient of deviation) is set by the sum of the signals' power, proportional to $\lambda_e N_e^2 + \lambda_i N_i^2$ in our case of matched synaptic constants. The reproducibility (signal-to-noise ratio or reliability) is set by the relative contributions of the excitatory and inhibitory signals to the output mean and variance. The individual signals can be changed without affecting output means or variabilities by carefully balanced adjustments to the synapses' constitutive parameters (e.g., λ_e , λ_i , N_e , and N_i). This tuning would not be possible if synaptic inputs were actually current based, and cannot be accomplished with current-input models.

ACKNOWLEDGMENTS

We thank H. S. Colburn for crucial discussions about the analytical methods used, and S. Epstein and K. P. Lillis for helpful discussions and reading an earlier version of this manuscript. An anonymous reviewer was extremely helpful in strengthening the theoretical results. This work was supported by NIH R01 MH61604 and R01 NS34425 (J.A.W.).

¹W. R. Softky and C. Koch, "The highly irregular firing of cortical cells is inconsistent with temporal integration of random EPSPs," *J. Neurosci.* **13**, 334–350 (1993).

²M. N. Shadlen and W. T. Newsome, "The variable discharge of cortical neurons: implications for connectivity, computation and information coding," *J. Neurosci.* **18**, 3870–3896 (1998).

³W. Bair, "Spike timing in the mammalian visual system," *Curr. Opin. Neurobiol.* **9**, 447–453 (1999).

⁴M. Bazhenov, I. Timofeev, M. Steriade, and T. J. Sejnowski, "Self-sustained rhythmic activity in the thalamic reticular nucleus mediated by depolarizing GABA A receptor potentials," *Nat. Neurosci.* **2**, 168–174 (2001).

⁵P. N. Steinmetz, A. Roy, P. J. Fitzgerald, S. S. Hsiao, K. O. Johnson, and E. Niebur, "Attention modulates synchronized neuronal firing in primate somatosensory cortex," *Nature* **404**, 187–190 (2000).

⁶C. Barrechea, M. Pedemonte, A. Nunez, and E. Garcia-Austt, "In vivo intracellular recordings of medial septal and diagonal band of Broca neurons: relationships with theta rhythm," *Exp. Brain Res.* **103**, 31–40 (1995).

⁷M. Penttonen, A. Kamondi, L. Acsady, and G. Buzsaki, "Gamma frequency oscillation in the hippocampus of the rat: intracellular analysis *in vivo*," *Eur. J. Neurosci.* **10**, 718–728 (1998).

⁸E. A. Stern, D. Jaeger, and C. J. Wilson, "Membrane potential synchrony of simultaneously recorded striatal spiny neurons *in vivo*," *Nature* **394**, 475–478 (1998).

⁹E. Salinas and T. J. Sejnowski, "Impact of correlated synaptic input on output firing rate and variability in simple neuronal models," *J. Neurosci.* **20**, 6193–6209 (2000).

¹⁰G. Svirskis and J. Rinzel, "Influence of temporal correlation of synaptic input on the rate and variability of firing neurons," *Biophys. J.* **79**, 629–637 (2000).

¹¹H. Korn and D. S. Farber, "Quantal analysis and synaptic efficacy in the CNS," *Trends Neurosci.* **14**, 439–445 (1991).

¹²J. M. Bekkers, G. B. Richerson, and C. F. Stevens, "Origin of variability in quantal size in cultured hippocampal neurons and hippocampal slices," *Proc. Natl. Acad. Sci. U.S.A.* **87**, 5359–5362 (1990).

¹³A. A. Faisal, J. A. White, and S. B. Laughlin, "Ion-channel noise places limits on the miniaturization of the brain's wiring," *Curr. Biol.* **15**, 1143–1149 (2005).

¹⁴E. Schneidman, B. Freedman, and I. Segev, "Ion channel stochasticity may be critical in determining the reliability and precision of spike timing," *Neural Comput.* **10**, 1679–1703 (1998).

¹⁵A. D. Dorval and J. A. White, "Channel noise is essential for perithreshold oscillations in entorhinal stellate neurons," *J. Neurosci.* **25**, 10025–10028 (2005).

¹⁶F. S. Chance, L. F. Abbott, and A. D. Reyes, "Gain modulation from background synaptic input," *Neuron* **35**, 773–782 (2002).

¹⁷A. Destexhe, M. Rudolph, J.-M. Fellous, and T. J. Sejnowski, "Fluctuating synaptic conductances recreate *in vivo*-like activity in neocortical neurons," *Neuroscience* **107**, 13–24 (2001).

¹⁸M. J. E. Richardson, "Effects of synaptic conductance on the voltage distribution and firing rate of spiking neurons," *Phys. Rev. E* **69**, 051918 (2004).

¹⁹A. D. Dorval, D. J. Christini, and J. A. White, "Real-time linux dynamic clamp: a fast and flexible way to construct virtual ion channels in living cells," *Ann. Biomed. Eng.* **29**, 897–907 (2001).

²⁰H. P. Robinson and N. Kawai, "Injection of digitally synthesized synaptic conductance transients to measure the integrative properties of neurons," *J. Neurosci. Methods* **49**, 157–165 (1993).

²¹A. A. Sharp, M. B. O'Neil, L. F. Abbott, and E. Marder, "The dynamic clamp: artificial conductances in biological neurons," *Trends Neurosci.* **16**, 389–394 (1993).

²²P. H. E. Tiesinga, J. V. Jose, and T. J. Sejnowski, "Comparison of current-driven and conductance-driven neocortical model neurons with Hodgkin-Huxley voltage-gated channels," *Phys. Rev. E* **62**, 8413–8419 (2000).

²³A. Kuhn, A. Aertsen, and S. Rotter, "Neuronal integration of synaptic input in the fluctuation-driven regime," *J. Neurosci.* **24**, 2345–2356 (2004).

²⁴C. F. Stevens and A. M. Zador, "Input synchrony and the irregular firing of cortical neurons," *Nat. Neurosci.* **1**, 210–217 (1998).

²⁵A. Alonso and R. Klink, "Differential electroresponsiveness of stellate and pyramidal-like cells of medial entorhinal cortex layer II," *J. Neurophysiol.* **70**, 128–143 (1993).

²⁶C. Koch, *Biophysics of Computation: Information Processing in Single Neurons* (Oxford University Press, New York, 1999), p. 365.

²⁷M. Rudolph and A. Destexhe, "Characterization of subthreshold voltage fluctuations in neuronal membranes," *Neural Comput.* **15**, 577–618 (2003).

²⁸M. J. Richardson and W. Gerstner, "Synaptic shot noise and conductance fluctuations affect the membrane voltage with equal significance," *Neural Comput.* **17**, 923–947 (2005).

²⁹A. N. Burkitt, H. Meffin, and D. B. Grayden, "Study of neuronal gain in a conductance-based leaky integrate-and-fire neuron model with balanced excitatory and inhibitory synaptic input," *Biol. Cybern.* **89**, 119–125 (2003).

³⁰A. Destexhe, M. Rudolph, and D. Pare, "The high-conductance state of neocortical neurons *in vivo*," *Nat. Rev. Neurosci.* **4**, 739–751 (2003).

³¹N. Fourcaud-Trocme, D. Hansel, C. van Vreeswijk, and N. Brunel, "How spike generation mechanisms determine neuronal response to fluctuating inputs," *J. Neurosci.* **23**, 11628–11640 (2003).

- ³²B. Doiron, A. Longtin, N. Berman, and L. Maler, "Subtractive and divisive inhibition: effect of voltage-dependent inhibitory conductances and noise," *Neural Comput.* **13**, 227–248 (2001).
- ³³N. Brunel, F. S. Chance, N. Fourcaud, and L. F. Abbott, "Effects of synaptic noise and filtering on the frequency response of spiking neurons," *Phys. Rev. Lett.* **86**, 2186–2189 (2001).
- ³⁴L. J. Borg-Graham, C. Monier, and Y. Fregnac, "Visual input evokes transient and strong shunting inhibition in visual cortical neurons," *Nature* **393**, 369–373 (1998).
- ³⁵R. V. Jensen, "Synchronization of randomly driven nonlinear oscillators," *Phys. Rev. E* **58**, R6907–R6910 (1998).
- ³⁶P. H. E. Tiesinga, J.-M. Fellous, and T. J. Sejnowski, "Attractor reliability reveals deterministic structure in neuronal spike trains," *Neural Comput.* **14**, 1629–1650 (2002).
- ³⁷Z. F. Mainen and T. J. Sejnowski, "Reliability of spike timing in neocortical neurons," *Science* **268**, 1503–1506 (1995).
- ³⁸J. D. Hunter, J. G. Milton, P. J. Thomas, and J. D. Cowan, "Resonance effect for neural spike time reliability," *J. Neurophysiol.* **80**, 1427–1438 (1998).
- ³⁹B. W. Knight, "Dynamics of encoding in a population of neurons," *J. Gen. Physiol.* **59**, 734–766 (1972).
- ⁴⁰S. Schreiber, J.-M. Fellous, P. Tiesinga, and T. J. Sejnowski, "Influence of ionic conductances on spike timing reliability of cortical neurons for suprathreshold rhythmic inputs," *J. Neurophysiol.* **91**, 194–205 (2004).
- ⁴¹R. R. de Ruyter van Steveninck, G. D. Lewen, S. P. Strong, R. Koberle, and W. Bialek, "Reproducibility and variability in neural spike trains," *Science* **275**, 1805–1808 (1997).
- ⁴²E. Schneidman, I. Segev, and N. Tishby, "Information capacity and robustness of stochastic neuron models," in *Advances in Neural Information Processing Systems* (M.I.T. Press, Cambridge, 2000), p. 12.
- ⁴³J.-M. Fellous, P. H. E. Tiesinga, P. J. Thomas, and T. J. Sejnowski, "Discovering spike patterns in neuronal responses," *J. Neurosci.* **24**, 2989–3001 (2004).
- ⁴⁴S. D. Reich, J. D. Victor, B. W. Knight, T. Ozaki, and E. Kaplan, "Response variability and timing precision on neuronal spike trains *in vivo*," *J. Neurophysiol.* **77**, 2836–2841 (1997).